Fuel 366 (2024) 131009

Contents lists available at ScienceDirect

Fuel

journal homepage: www.elsevier.com/locate/fuel

Full length article

Fuel effects on the electrostatic control of charged droplet trajectories

Andrea Giusti [a,*], Daniel Fredrich [b]

[a] Department of Mechanical Engineering, Imperial College London, South Kensington Campus, London, SW7 2AZ, United Kingdom
[b] Department of Engineering, University of Cambridge, Trumpington Street, Cambridge, CB2 1PZ, United Kingdom

ARTICLE INFO

Keywords:
Electrospray
Electrostatic field
Targeted evaporation
Rayleigh limit
Fuel flexibility
Electrohydrodynamics

ABSTRACT

The use of electrostatic fields to control the trajectory of charged droplets is investigated as a new technology to enhance mixing in liquid-fuelled combustors. The canonical configuration of a spray in crossflow is numerically studied with a focus on the effects of the fuel type on the onset of charge-induced breakup and droplet trajectories for a range of bulk flow velocities and electrostatic field strengths at conditions relevant to gas turbine applications. The investigated fuels are ethanol, n-heptane, and n-decane. Operational maps for each fuel are provided to assist the selection of the external electrostatic field required to achieve a balance between the drag and electrostatic forces, and enable a system design that considers fuel flexibility. The results demonstrate that the fuel type has an important impact on the diameter at which the charge-induced breakup is achieved, which mainly depends on the droplet equilibrium temperature. It is also shown that, for cases where the droplet net charge is fixed to a given fraction of the maximum possible charge (based on the Rayleigh limit), the temperature of the droplet at injection could be used as a parameter to control the onset of secondary breakup. Analysis of the strength of the electrostatic field necessary to achieve droplet stabilisation in a bulk flow shows that a balance between the electrostatic and drag forces can only be achieved for relatively low values of the bulk flow velocity, if the strength of the electrostatic field is kept below the breakdown limit of the carrier phase. This balance mainly depends on the droplet net charge and flow conditions, whereas the effect of the type of fuel on the drag force is less important. When the charge is imposed as a fraction of the maximum possible value at injection, for low values of the bulk flow velocity, the strength of the electrostatic field that balances the drag tends to become independent of the droplet diameter for a wide range of droplet sizes. Further investigation of the trajectories of evaporating droplets demonstrates that, although affected by the type of fuel through the evaporation rate, with the same settings of the electrostatic field, it is possible to achieve evaporation in a confined region for all the fuels and ambient conditions studied in this work once the initial droplet charge and initial droplet diameter are fixed. The present findings offer new insights for the development of future technologies for fuel preparation with enhanced mixing and fuel flexibility.

1. Introduction

Many energy systems used for transportation make use of liquid fuels to generate mechanical power and thrust. Although concerns about the global warming effects of carbon dioxide emissions call for an urgent development of technologies based on zero-carbon and renewable energy sources, in the short to medium term, the most promising solution to decarbonise hard-to-abate sectors such as aviation and shipping [1] is represented by the use of a range of sustainable fuels. These fuels include biofuels, which could allow for the achievement of net-zero carbon emissions, as well as e-fuels, i.e., hydrocarbon-based fuels synthesised through the use of electrical energy, possibly coming from renewable sources [2]. Typically, sustainable fuels are designed such that their use in conventional systems does not imply major changes to the combustion technology. In this way, current combustion technologies can still be used while decreasing the net amount of carbon dioxide released into the atmosphere. Although the use of sustainable fuels is the most practicable solution in the short term, there are still a number of technological issues, related to the liquid nature of the fuel and the necessity of controlling the mixing with the oxidiser, that limit their extensive use in current devices. Reducing the formation of pollutants (including particulates) while achieving flame stabilisation and fuel flexibility is one of the main challenges of current combustion technologies used in transportation, together with the necessity of minimising the weight and size of the engine. These challenges are predominantly addressed through the control of the fuel-air mixing, starting from a fine fuel atomisation and an optimised

* Corresponding author.
E-mail address: a.giusti@imperial.ac.uk (A. Giusti).

https://doi.org/10.1016/j.fuel.2024.131009
Received 26 October 2023; Received in revised form 10 January 2024; Accepted 16 January 2024
Available online 10 March 2024

design of the combustion chamber geometry and air flows such that a precise control of the local air-to-fuel ratio can be achieved [2–5]. Fine atomisation and turbulent mixing are typical strategies adopted to enable the quick formation of a homogeneous mixture, e.g., for the reduction of nitrogen oxide emissions. However, the design of the injection system, combustion chamber geometry, and air flows is often the result of a compromise between multiple requirements in terms of spray atomisation, droplet location, residence time, quick mixing, and flame stabilisation, which are related to a wide range of scales (in space and time) that characterise liquid breakup, evaporation, ignition, chemical reactions, and the formation of pollutants and particulates [6–10].

In the attempt of improving the overall performance of combustion technologies, the use of electromagnetic fields to control the reaction process has gained increased attention in recent years. In addition to the direct use of electromagnetic fields to enhance the flame and emission characteristics, e.g., via plasma-assisted combustion [11–13] or low-energy electromagnetic fields [14,15], the use of charged fuel droplets (i.e., electrosprays) to improve the atomisation and mixing has also been proposed [16,17]. Inducing an electric charge into the fuel droplets can improve the atomisation characteristics through a secondary breakup mechanism caused by charge repulsion within the liquid. As a charged droplet evaporates and its diameter decreases, repulsion forces inside the droplet become more and more dominant against the surface tension, until an instability is triggered either by aerodynamic interactions [18] or directly by charge repulsion (at the so-called Rayleigh limit [19]) causing the droplet to fragment into smaller child droplets. This phenomenon further reduces the evaporation time [18], possibly enabling an improved mixing between the fuel vapour and air. In addition, electric repulsion between different droplets promotes better inter-droplet separation with additional benefits on the fuel-air mixing [20,21]. The possibility of achieving control over the trajectory of droplets and over the size distribution of injected droplets has also been pointed out [21,22]. Effects of the charged droplets on the flame characteristics have also been studied, demonstrating that the presence of charges could have an impact on the shape and stability of the flame [23,24]. The technology used to create charged droplets depends on the electrical properties of the fuel (see e.g., [20]). For low conductivity fuels, such as diesel and kerosene, a charge injection technology has been developed [25,26]. In this technology, the total amount of charge injected in the spray depends on the injector configuration; it generally increases with increasing potential difference until partial breakdown of the liquid is reached [26]. Characterisation of the spray downstream of the injection location has shown that the droplet size and charge density of the droplets depend on the fuel properties, as well as on the geometry of the injector [20,26,27]. Efforts have been made over the years to increase the flow rate of fuel to reach values useful for practical combustion applications [28], as well as to increase the spray charge density and narrow down the droplet size distribution resulting from charge injection technology [20]. Charge injection of fuels characterised by high viscosity, e.g., biomass fuels, has also been investigated [21,29]. Advancements in the direction of enabling larger fuel flow rates in injection systems used for aviation are reported in Ref. [17], where fuel injectors capable of producing large quantities of charged fuel droplets are evaluated. An alternative is represented by the use of multiple injectors, which, in principle, could also enable staged combustion [30] and an enhanced potential for fuel flexibility. However, there is still uncertainty over important aspects involved in electrospray atomisation, including the characteristics of the droplets after primary breakup, the actual mass of injected fuel that is involved in the charged-induced secondary breakup, and the charge density of the droplets resulting from secondary atomisation. More in general, for a given injector geometry, a better characterisation of the droplet size and charge distributions as a function of fuel properties must be established to further improve the control of electrospray technologies and determine to what extent the use of electrosprays could lead to improvements in the fuel preparation.

A significant step towards the use of electrohydrodynamic effects to control the fuel-air mixing in energy systems was recently reported by Fredrich et al. [16]. The combination of electrosprays and external electrostatic fields to modulate the dynamics of charged fuel droplets, and thereby the fuel location, was proposed as a new technology referred to as *targeted evaporation*. By applying an electrostatic force to counteract the drag force imposed by a bulk flow of air, this technology was shown to have the potential of increasing the residence time of droplets within a confined region, thus allowing for full pre-evaporation of the fuel before the droplets reach the flame zone. The investigation focused exclusively on kerosene fuel. However, in a scenario where fuel flexibility and the use of alternative sustainable fuels are of paramount importance to decarbonise the transportation sector, there is a necessity to further examine this new technology for a range of fuels to better understand its limitations and range of applicability.

To provide further insight into the use of electrosprays and electrostatic forces to enhance the fuel preparation process, fuel effects on the trajectory of droplets in a spray in crossflow under external electrostatic fields are investigated. The objectives of this study are to: (i) investigate the effect of the fuel type on the onset of the droplet Rayleigh instability for a range of initial droplet charge densities, initial droplet diameters, and ambient conditions relevant to gas-turbine applications; and (ii) identify the range of bulk flow velocities and strengths of the external electrostatic field that could enable complete evaporation in a confined space as a function of the fuel type. Three different fuels are considered in this work, namely ethanol (a biofuel), n-heptane, and n-decane. The first objective is addressed through an evaluation of the evaporation timescales and a theoretical analysis of the effect of fuel properties on the Rayleigh limit for the specific fuels and ambient conditions investigated here. This analysis provides fundamental droplet characteristics, including total evaporation time and minimum droplet diameter before fragmentation, to be used later on in the analysis of droplet trajectories and balance between drag and electrostatic forces. The second objective is addressed by means of an a-priori balance between drag and electrostatic forces and a computation of droplet trajectories using a deterministic model. The paper is organised as follows. First, the test case configuration and investigated conditions are presented. Then, the methods utilised in this work are described, followed by the results and their discussion. A summary and conclusions close the paper.

2. Configuration and investigated cases

The spray in crossflow already investigated in Ref. [16] is studied here as a canonical configuration to evaluate the competing effects of the drag and electrostatic forces. This configuration represents a premixing section to be located upstream of the flame to ensure control over the preparation of the fuel-air mixture. A schematic of the investigated geometry is provided in Fig. 1. The spray is injected perpendicularly into a bulk flow between two parallel, horizontal walls. The distance between the two walls is assumed to be sufficient to avoid any impact of the droplets on the walls. From a practical point of view, given a specific flow condition (i.e., bulk flow velocity and density), this distance could be adjusted to ensure the desired mass flow rate. For the sake of post-processing, a two-dimensional (2D) Cartesian frame of reference with x-axis aligned with the bulk flow direction, vertical y-axis, and origin at the spray injection location is utilised.

Three different combinations of ambient air pressure, p_g, and temperature, T_g, are considered, as summarised in Table 1. Each case represents a condition relevant to real engine applications, where the bulk flow preheating is a consequence of the adiabatic compression of air. The initial temperature of the fuel, $T_{d,0}$, is equal to 320 K at all conditions, and the injection velocity of the droplets, $\boldsymbol{u}_{d,0}$, points in the vertical upward direction with a magnitude of 20 m/s. An external electrostatic field is imposed to generate a force on the charged droplets in the direction opposite to the bulk flow. In practice, such

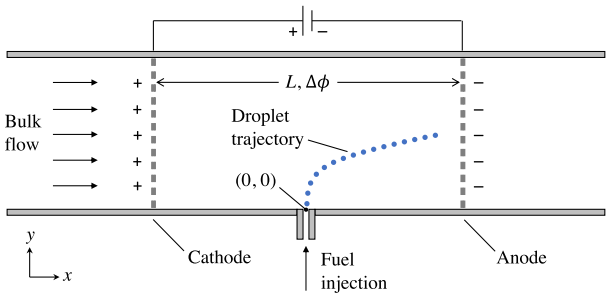

Fig. 1. Schematic of the canonical spray in crossflow configuration investigated in this work including the use of an electrospray and an external electrostatic field. The external electrostatic field is assumed to be generated by two parallel plates. The distance, L, between the parallel plates and the electrical potential difference, $\Delta\phi$, between them should be adjusted such that $|\boldsymbol{E}| = \Delta\phi/L$. The anode and cathode, as depicted in this schematic, refer to the specific case of negatively-charged droplets.

Table 1
Gas-phase conditions and corresponding initial droplet temperature and velocity magnitude investigated in this work.

Case	p_g [bar]	T_g [K]	$T_{d,0}$ [K]	$\lvert\boldsymbol{u}_{d,0}\rvert$ [m/s]
(a)	5	470	320	20
(b)	10	575	320	20
(c)	20	700	320	20

external electrostatic field could be generated by a pair of parallel, electrically-conductive, perforated plates (see e.g., Ref. [31]) installed normal to the bulk flow inside the channel. For each case, a range of droplet diameters and gas-phase bulk flow velocities up to 500 μm and 100 m/s, respectively, are investigated. In addition, different initial droplet charges are considered up to the theoretical limit related to the Rayleigh instability [19]. Cases either with a fixed initial droplet charge density or with a droplet charge expressed as a fraction of the maximum theoretical value are investigated. This is further detailed in the remainder of the paper. For each condition, the corresponding strength of the external electrostatic field needed to obtain a stationary droplet (i.e., to reach spatial equilibrium in the absolute frame of reference) is computed from a balance of forces acting on the droplet. Note that the vertical penetration of the droplet is mainly the result of the initial droplet velocity. If a different penetration is desired for a given droplet size, then either a different initial droplet velocity or an electrostatic field in the vertical direction can be used [16].

3. Methods

To study the trajectory of charged droplets, the deterministic model introduced in Ref. [16] is further developed to include droplet evaporation. In addition, the droplet diameter at which the Rayleigh limit is achieved is evaluated. In the following, the deterministic model used to compute the trajectory of charged droplets is first discussed. Then, the method used to evaluate the evaporation rate constant is presented, followed by a discussion of the Rayleigh limit for secondary breakup.

3.1. Deterministic model

A numerical framework for computing the trajectory of a single, non-evaporating droplet under the effect of an external electrostatic field in 2D space was recently proposed in Ref. [16]. The model is based on the integration of Newton's second law to solve for droplet velocity and position, and includes both the applied external electrostatic force and the drag force induced by a bulk flow surrounding the droplet. All other forces acting on the droplet, including the added-mass force, are neglected. The electrostatic force is simply the product of the droplet net charge and the external electrostatic field:

$$\boldsymbol{F}_E = q_d\,\boldsymbol{E}, \tag{1}$$

where $\boldsymbol{E}$ is the applied external electrostatic field and q_d is the droplet net charge, which is given by the droplet charge density, $\rho_{q,d}$, multiplied by the droplet volume, V_d. During droplet evaporation, the net charge is assumed to be constant [32], i.e., there is no charge transfer into the gas phase. This is due to the much slower charge decay rate in comparison to the droplet evaporation rates.

The drag force, under the assumption of a spherical droplet, is computed as:

$$\boldsymbol{F}_D = \frac{1}{8}\,\rho_g\,\boldsymbol{u}_{\mathrm{rel}}\,|\boldsymbol{u}_{\mathrm{rel}}|\,C_D\,\pi\,d^2, \tag{2}$$

where ρ_g is the density of the gas phase, d is the droplet diameter, and $\boldsymbol{u}_{\mathrm{rel}}$ is the relative velocity between the bulk flow and the droplet. For the simulation of the droplet trajectories in the channel flow configuration discussed in Section 2, the velocity profile of the bulk flow is assumed to be uniform; as if the air stream is supplied from a large plenum and the droplet injection is very close to the entrance of the channel. In addition, droplet trajectories are computed under the assumption of one-way coupling, i.e., no effects of the droplet on the gas phase. The drag coefficient, C_D, for spherical droplets is evaluated using the relation [33,34]:

$$C_D = \begin{cases} 0.424, & \text{if } \mathrm{Re}_d > 1000, \\ \frac{24}{\mathrm{Re}_d}\left(1 + \frac{\mathrm{Re}_d^{2/3}}{6}\right), & \text{otherwise}, \end{cases} \tag{3}$$

where $\mathrm{Re}_d = \rho_g\,|\boldsymbol{u}_{\mathrm{rel}}|\,d/\mu_{g,r}$ is the droplet Reynolds number and $\mu_{g,r}$ is the dynamic viscosity of the gas phase computed at certain reference conditions. For evaporating droplets, $\mu_{g,r}$ is evaluated at the reference conditions given by the '1/3-rule', as detailed in Ref. [34]. This allows us to include into the model the effect of evaporation, which determines a change in gas properties in the region around the droplet, on the drag force. The dynamic viscosity of the air is computed using correlations from Ref. [35], whereas the dynamic viscosity of the fuel vapour is evaluated using the method in Ref. [36]. An equilibrium assumption is invoked to compute the fuel vapour partial pressure at the droplet surface, which is used to evaluate the fuel mass fraction in the reference conditions. Correlations from Ref. [37] are used to evaluate the vapour pressure of each fuel. The viscosity of the gas mixture is computed according to the method of Wilke [38] with Herning and Zipperer approximation, as discussed in Ref. [39]. Note that no explicit correction of the drag coefficient to account for the influence of the Stefan flow (e.g., Refs. [40,41]) has been used in this work. This follows the recommendation of Ref. [42] in the specific case of Re_d computed with a dynamic viscosity evaluated at the '1/3-rule' reference conditions.

In the present work, the evolution of the droplet diameter over time is modelled using a simple d^2-law:

$$d = \begin{cases} d_0, & \text{if } t < \tau_{\mathrm{hp}}, \\ \sqrt{d_0^2 - K\,\left(t - \tau_{\mathrm{hp}}\right)}, & \text{otherwise}, \end{cases} \tag{4}$$

where t is the time from injection, d_0 is the initial droplet diameter, K represents the evaporation rate constant, and τ_{hp} is the duration of the initial heat-up period. The evaporation rate constants at each ambient condition and for each fuel of interest are evaluated from single-droplet computations, as described in Section 3.2. The duration of the heat-up period is computed as $\tau_{\mathrm{hp}} = \tau_{\mathrm{ev}} - d_0^2/K$ [43], where τ_{ev} is the total evaporation time evaluated from single-droplet computations. During the heat-up period, the temperature of the droplet is assumed to increase linearly from $T_{d,0}$ to the equilibrium value, $T_{d,\mathrm{eq}}$ (wet bulb temperature), also taken from the single-droplet computations. It should be noted that the present formulation used for evaporation does not consider the effect of a relative velocity between the droplet and the gas phase, i.e., the effect of a Re_d greater than zero on the evaporation rate is not included in the model. The presence of a relative velocity between the droplet and the gas phase generally leads to an increase

of the evaporation rate and, therefore, shorter droplet lifetimes. Non-zero Re_d effects are estimated in the Appendix, which also demonstrates that the increase of the evaporation rate with Re_d further supports the main conclusions of this work regarding the possibility of confining evaporation in the vicinity of the injection location. Note also that in the present formulation, it is assumed that the presence of a net charge in the droplet does not affect the mass transfer at the droplet-gas interface. This assumption is consistent with previous work [18,44]. In addition, secondary breakup is not included in the computation of droplet trajectories. Evaluation of secondary breakup effects should be addressed in future studies, e.g., starting from the models proposed in Refs. [18,44].

3.2. Evaporation rate constant

To evaluate the evaporation time scale and related evaporation rate constant, K, to be used in the d^2-law, as well as the droplet equilibrium temperature, single droplet computations in a quiescent medium are performed using the methods described in Refs. [45,46]. Conservation equations for both the droplet and the gas phase, under the assumption of spherical symmetry, are solved with interface conditions to ensure exchange of mass and energy between the two phases. Thermodynamic equilibrium is assumed at the droplet surface, i.e., the partial pressure of the fuel vapour is taken equal to the saturation pressure at the droplet temperature. The reader is referred to Refs. [45,46] and the references therein for more details regarding the numerical method. For all three fuels, the liquid thermodynamic properties (e.g., vapour pressure, latent heat, and heat capacity), which are very important for the computation of the evaporation rates, are evaluated using correlations taken from Ref. [37]. The solver allows us to extract the time evolution of the droplet diameter, in addition to the radial distribution of the temperature and vapour around the droplet, as well as the radial distribution of the temperature inside the droplet. From the time evolution of the square of the droplet diameter, the evaporation rate constant, K, can be estimated. In this work, K is computed by linearly interpolating the points corresponding to $d^2/d_0^2 = 0.8$ and $d^2/d_0^2 = 0$ in the plots shown in Fig. 3, which reports the square diameter against time (see also Ref. [43]). In addition, the droplet equilibrium temperature, $T_{d,\mathrm{eq}}$, is evaluated as the average temperature at the droplet surface in the time period corresponding to $d^2/d_0^2 < 0.8$.

For each fuel, the capability of the solver to predict the total evaporation time has been assessed through comparisons with data from the literature. In particular, for ethanol we performed an extensive comparison with data at various ambient pressures (up to 20 bar) and temperatures (up to 1000 K) published in Ref. [47]. The droplet temperature at equilibrium (after the initial heat-up period) was also compared. This assessment showed an excellent agreement, yielding deviations within 5% of the reference values. As far as n-heptane and n-decane are concerned, an assessment in terms of the total evaporation time was performed against data from Ref. [48] at low and high ambient temperatures, and for a range of ambient pressures (up to 20 bar). For both fuels, a very good agreement with the reference data was obtained at elevated temperatures ($T_g \sim 750$ K), whereas an over-prediction of the evaporation time, with deviations of around 10%, was found at lower temperatures ($T_g \sim 450$ K). Overall, the assessment can be considered satisfactory, demonstrating the reliability of the framework (i.e., the applied method and selected correlations for the properties of the liquid) used in the present investigation.

3.3. Charge-induced breakup

There is a maximum limit, usually referred to as the *Rayleigh limit*, to the amount of charge that a droplet of a given fuel and diameter can contain [19]. If the amount of charge goes beyond this limit, the repulsion forces inside the droplet may cause instabilities that will eventually lead to the fragmentation of the droplet (i.e., a breakup induced by electric forces). A fuel droplet is said to be at the Rayleigh stability limit when the net charge reaches a value of [48,52]:

$$q^* = 8\pi \left(\varepsilon_0 \sigma \frac{d^3}{8}\right)^{1/2}, \tag{5}$$

where σ is the surface tension of the fuel and ε_0 is the vacuum permittivity. In this work, we deal with a droplet with a given initial charge. For the droplet to exist, the charge must be below the critical value imposed by Eq. (5). As the droplet evaporates, the diameter decreases until the Rayleigh condition is achieved, which is followed by instability growth and breakup. For a given initial droplet charge density, $\rho_{q,d,0}$, the value of the critical diameter, d^*, at which instability is triggered is given by (this is obtained by rearranging Eq. (5) after imposing the initial charge density):

$$d^* = \frac{d_0^2}{2}\left(\frac{\rho_{q,d,0}^2}{36\varepsilon_0\sigma}\right)^{1/3}. \tag{6}$$

It should be noted that once the initial droplet charge density, $\rho_{q,d,0}$, is fixed, the critical diameter depends on both the initial droplet diameter, d_0, and the type of fuel through the surface tension. In the evaluations done in this work, the surface tension for n-heptane and n-decane is computed according to the Brock-Bird method [37,50], whereas for ethanol, the correlation from Gonçalves et al. [49] has been used. Fig. 2 shows a comparison between the surface tension obtained from the correlations and some reference experimental data [51], demonstrating the reasonable accuracy of the surface tension values used in the present work. In the following, the surface tension of the fuel a long time after injection is evaluated at the droplet equilibrium temperature, which is directly extracted from the single droplet computations.

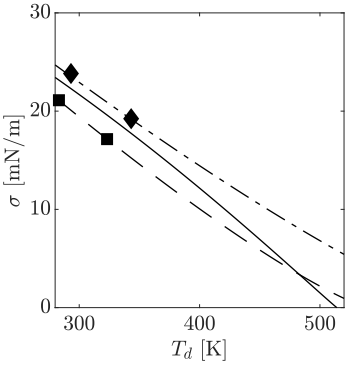

Fig. 2. Surface tension as a function of the droplet temperature for the three fuels investigated in this work: ethanol ——, n-heptane — —, n-decane – · –. The correlation used for ethanol was validated in Ref. [49]. The Brock-Bird method [37,50] is used for both n-heptane and n-decane, and is compared here to experimental validation points from Ref. [51], represented by square and diamond markers for n-heptane and n-decane, respectively.

Table 2
Fundamental relations between the droplet diameter, surface tension, and charge density for a droplet with a net charge of $q_d = q_0^*/a$, where q_0^* is the critical charge evaluated using Eq. (5) at the droplet injection conditions. The relations were derived through manipulation of Eqs. (5) and (6). d_0 and σ_0 are the diameter and surface tension at injection; d^* is the droplet diameter at the Rayleigh limit; $\rho_{q,d,0}$ and ρ_{q,d^*} are the droplet charge densities at injection and Rayleigh limit conditions, respectively; σ is the surface tension corresponding to the droplet temperature when the Rayleigh limit is reached.

Quantity	Relation
Initial droplet charge density	$\lvert\rho_{q,d,0}\rvert = \frac{6}{a}\left(\frac{8\varepsilon_0\sigma_0}{d_0^3}\right)^{1/2}$
Droplet charge density at the Rayleigh limit	$\lvert\rho_{q,d^*}\rvert = \frac{6a\sigma}{\sigma_0}\left(\frac{8\varepsilon_0\sigma_0}{d_0^3}\right)^{1/2}$
Ratio between the critical and initial diameter	$\frac{d^*}{d_0} = \left(\frac{\sigma_0}{a^2\sigma}\right)^{1/3}$

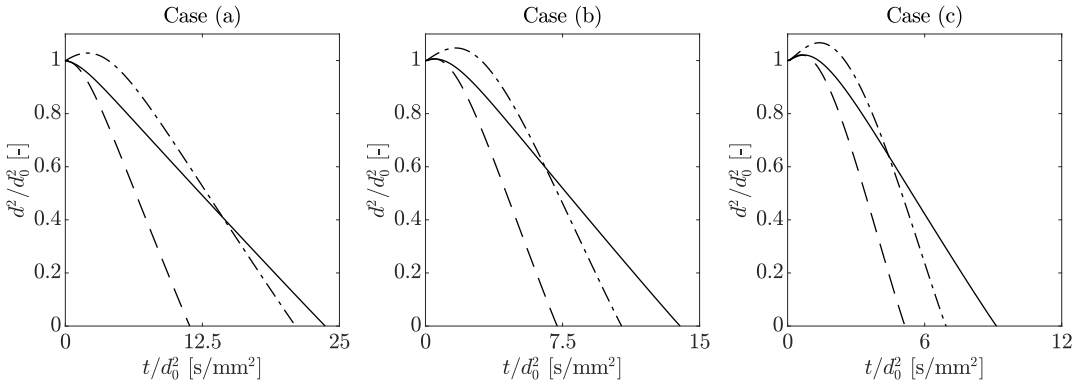

Fig. 3. Time evolution of the droplet diameter for the various fuels at the three conditions investigated in this work: ethanol ——, n-heptane — —, n-decane — · —.

There is evidence in the literature that for electrosprays, the net charge contained in a droplet of diameter d_0 after atomisation is about half the value given by the Rayleigh limit (i.e., half the value given by Eq. (5)) or lower [27,53,54]. Therefore, in addition to cases with an imposed initial droplet charge density, it is also sensible to investigate cases with a droplet charge set equal to a fraction of q^* evaluated at the droplet injection conditions, i.e., $q_d = q_0^*/a = \pi(8\varepsilon_0\sigma_0 d_0^3/a^2)^{1/2}$, where σ_0 is the surface tension at $T_{d,0}$ and $a > 1$. Note that in the remainder of the paper q_0^* will be used to indicate the critical charge evaluated at the droplet injection conditions. For each value of a, it is possible to find relations for the initial droplet charge density, critical diameter, and droplet charge density at the Rayleigh limit as a function of the injection droplet diameter, d_0, and surface tension, σ_0. These relations are summarised in Table 2. In the following, evaluations with both imposed initial charge density and imposed $q_d = q_0^*/a$ will be performed. It is important to point out that the presence of an external electric field may determine a redistribution of charges at the droplet surface, with an effect on the onset of charge-induced fragmentation [55]. This effect is not taken into account in the present study. In addition, when a droplet is in relative motion with respect to the surrounding gas, the presence of charges contributes to reducing the stabilising effect of surface tension, possibly favouring instabilities triggered by the aerodynamic interactions (see e.g., [18,22]).

4. Results and discussion

4.1. Evaporation time scale

Fig. 3 shows the time evolution of the droplet diameter for the various fuels at the three ambient conditions investigated in this work. After an initial heat-up period, all the fuels exhibit, with good approximation, a linear decrease of the square of the droplet diameter, therefore justifying the applicability of the d^2-law after the initial transient. A comparison of the behaviour of the various fuels shows that n-heptane is the fuel characterised by the shortest total evaporation time, whereas ethanol, despite the relatively quick heat-up period, is the fuel with the longest total evaporation time. As far as n-decane is concerned, droplets of this fuel are characterised by a relatively long heat-up period. However, after the equilibrium temperature is reached, the evaporation process is relatively quick. This is further demonstrated in Fig. 4, where both the evaporation rate constant, K (extracted from the d^2-law), and the droplet equilibrium temperature (i.e., the droplet temperature after the heat-up period) are shown for each of the cases investigated here. n-Heptane is the fuel with the highest evaporation rate constant in each ambient condition, immediately followed by n-decane. The highest equilibrium temperature is reached by n-decane. This higher temperature is related to the lower volatility of n-decane compared to the other fuels, which implies the necessity of a higher surface temperature to attain a fuel vapour pressure high enough to achieve equilibrium

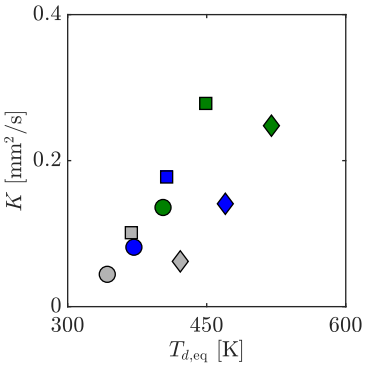

Fig. 4. Evaporation rate constant and droplet equilibrium temperature for the various fuels at the three conditions investigated in this work. Marker shapes indicate the fuel: circles are used for ethanol, squares for n-heptane, diamonds for n-decane. Colours are used to distinguish the various conditions: grey for Case (a), blue for Case (b), green for Case (c). (For interpretation of the references to colour in this figure legend, the reader is referred to the web version of this article.)

between the heat and mass transfer with the surrounding medium. The higher droplet temperature, together with the fuel thermal properties, leads to higher peak values of the droplet diameter and a longer heat-up period, as already observed with reference to Fig. 3. On the contrary, ethanol droplets are characterised by a very high volatility, which leads to relatively low equilibrium temperatures and a short heat-up period. By comparing ethanol with n-decane, this short heat-up period explains the faster evaporation of the ethanol droplet in the first part of the transient. However, the lower value of the ethanol evaporation rate constant eventually leads to a longer total evaporation time for the ethanol droplets. From a practical point of view, a quicker evaporation of ethanol droplets (compared to n-decane droplets) in the vicinity of the injector may be expected. However, ethanol requires a longer residence time to complete evaporation. Note that in this discussion, we have not considered any increase of the fuel vapour mass fraction in the gas phase (far from the droplet surface – i.e., the discussion is only valid in the limit of a very dilute spray), which would decrease the evaporation rates.

4.2. Rayleigh limit

For the sake of developing technologies based on the use of electrosprays, it is important to analyse (for each fuel and in each investigated ambient condition) the critical diameter, d^*, below which droplet instability and breakup driven by repulsion forces between charges is expected. We first investigate the behaviour of d^* as a function of d_0 for imposed values of the initial droplet charge density. Then, cases with a droplet net charge equal to a fraction of q_0^* are analysed. By making

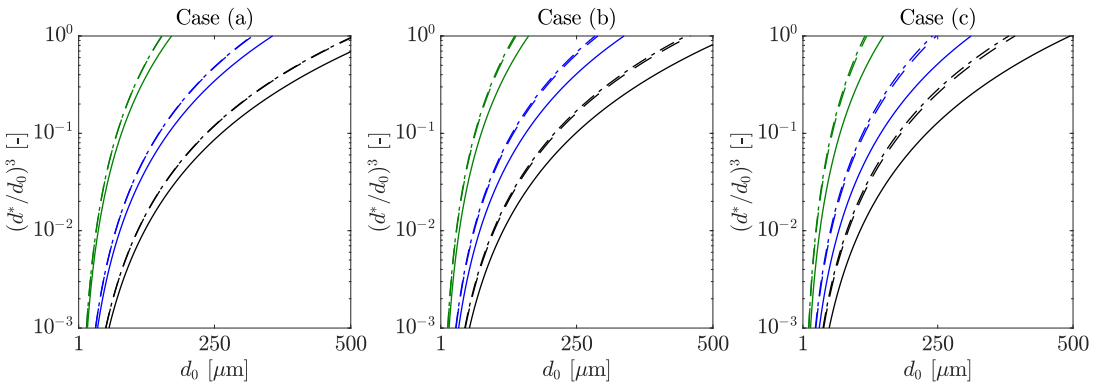

Fig. 5. Ratio between the droplet volume when the Rayleigh limit is reached and the initial volume of the droplet as a function of the initial droplet diameter for the various fuels at the three ambient conditions investigated in this work: ethanol ——, n-heptane — —, n-decane – · –. Different colours indicate different initial droplet charge densities: black lines for $|\rho_{q,d,0}| = 0.5$ C/m^3, blue lines for $|\rho_{q,d,0}| = 1$ C/m^3, green lines for $|\rho_{q,d,0}| = 3$ C/m^3. Note that the dashed and dash-dotted lines in Case (a) are overlapping. (For interpretation of the references to colour in this figure legend, the reader is referred to the web version of this article.)

use of Eq. (6), Fig. 5 shows the critical diameter as a function of the initial droplet diameter for different values of the initial droplet charge density. Note that the equilibrium temperatures reported in Fig. 4 are used to evaluate the surface tension of each fuel when the critical diameter is reached. The critical diameter is reported as $(d^*/d_0)^3$, which provides an estimate of the fraction of the droplet mass, compared to its initial mass, involved in secondary atomisation. It is worth noting that the balance of forces described in the next sections is based on the assumption of no secondary breakup. After secondary breakup, the net charge in each child droplet will be a fraction of the initial charge, and the electrostatic force acting on these droplets will be lower compared to the value before breakup. Fig. 5 demonstrates that for all fuels and for initial charge densities lower or equal to 1 C/m^3, an initial droplet diameter lower than 75 μm implies that only a small fraction (< 3.5%) of the initial mass is involved in secondary atomisation at all ambient conditions investigated here. The fraction is smaller in Case (a) and increases with increasing droplet equilibrium temperature, i.e., in Case (c) – this is due to changes in the surface tension of the fuel. However, for high initial droplet charge densities, e.g., 3 C/m^3 as shown in Fig. 5, a significant part of the initial mass could be involved in secondary atomisation also for relatively low initial droplet diameters. Note that droplets with $d^*/d_0 > 1$ cannot exist. Therefore, Fig. 5 also provides an upper limit to the initial droplet diameter for each value of the initial droplet charge density. Comparing the various fuels with each other, we observe that for a given initial droplet diameter and a given initial droplet charge density, ethanol is characterised by the lowest critical diameter in all of the investigated gas-phase conditions. This is related to its higher surface tension at the equilibrium temperature. It should also be noted that n-heptane and n-decane exhibit similar critical diameters, despite being characterised by large differences in equilibrium temperature at all gas-phase conditions.

If the net charge of the droplets is imposed as a fraction of q_0^*, the initial droplet charge density becomes a function of the initial droplet diameter (see also Table 2). Fig. 6 shows the initial charge density and the charge density of the droplet once the critical diameter is reached (with the net charge fixed at the initial value) as a function of d_0 for the three fuels and ambient conditions investigated in this work and in the case of a droplet net charge equal to $q_d = q_0^*/2$. The charge density decreases with increasing droplet diameter, demonstrating that smaller droplets are able to carry much more charge per unit volume. In addition, the initial charge density is similar for all the fuels investigated in this work, which is a consequence of the similar values of surface tension at the droplet initial temperature (cf. Fig. 2). Conversely, the charge density when the droplet reaches the Rayleigh limit is much more dependent on the fuel type. The results shown in Fig. 6 have been obtained by using the droplet equilibrium temperature (cf. Fig. 4) to evaluate the surface tension at the Rayleigh limit. Ethanol droplets reach the highest values of charge density, which implies a lower droplet diameter at the onset of the charge-driven breakup. On the contrary, n-decane droplets show the lowest charge density at breakup. This is mainly a consequence of the different values of surface tension at the equilibrium temperature. From the relations in Table 2, the values of d^*/d_0 depend solely on a and the ratio of the fuel surface tension at injection, σ_0, over the fuel surface tension, σ, when the critical diameter is reached. The values of d^*/d_0 obtained with σ computed at the droplet equilibrium temperature are shown in Fig. 7 for $q_d = q_0^*/2$ (i.e., $a = 2$). In all ambient conditions, ethanol droplets are characterised by the lowest critical diameter, followed by the n-heptane and n-decane droplets. The decrease in surface tension with increasing droplet temperature leads to an increase in $(d^*/d_0)^3$ compared to the value $(d^*/d_0)^3 = 1/a^2 = 0.25$ obtained in the case of constant surface tension. This implies that, as the droplet heats up after injection, the Rayleigh limit is achieved earlier compared to a constant droplet temperature case. The effect is particularly significant for n-decane droplets, which experience the largest differences in temperature between injection and equilibrium. It is interesting to note that in Case (c), the ratio d^*/d_0 is very close to 1.0 for the n-decane droplets. This means that the droplets may undergo charge-induced breakup shortly after the heat-up period. Note that the results in Fig. 7 depend on the initial droplet net charge (i.e., on the values of a) and injection temperature (which affects the value of σ_0). The above considerations highlight the importance of the fuel properties and injection temperature on the onset of droplet fission induced by charge repulsion. In the case of an initial net charge equal to a fixed fraction of q_0^*, the droplet injection temperature could be used as a design parameter to change the initial net charge in the droplets. Given that the equilibrium temperature only depends on the gas-phase conditions and fuel type, it is also possible to modulate the ratio d^*/d_0 by means of $T_{d,0}$ for each ambient condition and each fuel. This is shown in Fig. 8 for $q_d = q_0^*/2$. The effect of $T_{d,0}$ is greater for the fuels that experience a greater change in droplet temperature during the heat-up period. With reference to Case (c) and n-decane droplets, it is interesting to note that for low values of the initial droplet temperature, the ratio d^*/d_0 becomes greater than 1.0. This condition is not physically possible and the droplet is expected to break up during the heat-up period, as the surface tension decreases, making it incapable of stabilising the repulsion forces between the charges. Note that the equilibrium temperature considered here has been evaluated in quiescent conditions. In case of a relative velocity between the droplet and the gas phase, different values of the equilibrium temperature may be found. The increase of charge density (of the spray) with decreasing temperature of the fuel has been demonstrated experimentally for charge injection atomisation of diesel [56]. Note that fuel temperature also affects the physical properties of the fuel, such as the dynamic viscosity, which could have an effect on primary atomisation [56].

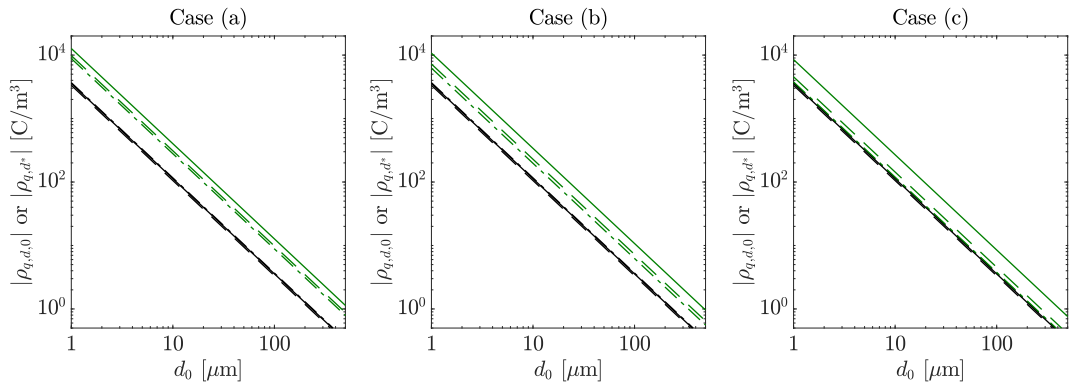

Fig. 6. Initial droplet charge density, $\rho_{q,d,0}$, (black colour) and charge density when the droplet has reached the critical diameter, ρ_{q,d^*}, (green colour) as a function of the initial droplet diameter, d_0, for an initial net charge equal to $q_0^*/2$. The various fuels at the three conditions investigated in this work are indicated by different lines: ethanol ——, n-heptane — —, n-decane – · –. (For interpretation of the references to colour in this figure legend, the reader is referred to the web version of this article.)

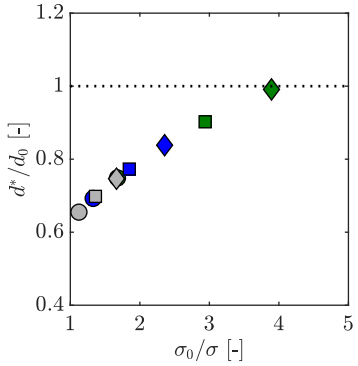

Fig. 7. d^*/d_0 over σ_0/σ for a net charge of the droplet equal to $q_0^*/2$ for the various fuels at the three conditions investigated in this work. Marker shapes indicate the fuel: circles are used for ethanol, squares for n-heptane, diamonds for n-decane. Colours are used to distinguish the different ambient conditions: grey for Case (a), blue for Case (b), green for Case (c). (For interpretation of the references to colour in this figure legend, the reader is referred to the web version of this article.)

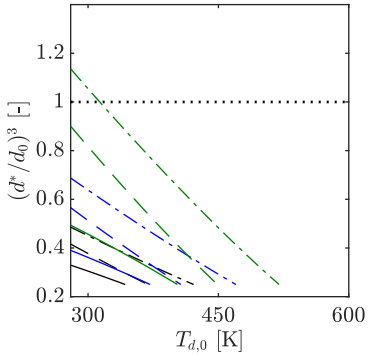

Fig. 8. $(d^*/d_0)^3$ as a function of the initial droplet temperature, $T_{d,0}$, for the various fuels at the three conditions investigated in this work and with an initial net charge of the droplet equal to $q_0^*/2$. The fuels are indicated by different lines: ethanol ——, n-heptane — —, n-decane – · –. Colours are used to distinguish the different ambient conditions: black for Case (a), blue for Case (b), green for Case (c). Only initial droplet temperatures below the equilibrium value are considered. (For interpretation of the references to colour in this figure legend, the reader is referred to the web version of this article.)

To improve the degree of control, the characterisation of electrospray atomisation needs to be improved. Research in the future should focus on better identifying what fraction of the net charge given by the Rayleigh limit is left in the droplet after atomisation, as a function of the fuel properties and atomiser geometry [22,27,57].

4.3. Operational maps

The intention of this section is to estimate the strength of the electrostatic field necessary to reach a balance between drag and electrostatic forces for a range of bulk flow velocities, droplet diameters, and droplet charge densities. For the sake of simplicity, let us consider an evaporating droplet of diameter d, which has already reached the equilibrium temperature, immersed in a steady and uniform flow with velocity $\boldsymbol{u}_g$. We assume an external electrostatic field aligned with the direction of the gas-phase velocity such that the electrostatic force acting on the droplet is opposite to the direction of the flow (e.g., if the droplet is negatively charged, then the electric field is in the same direction as the flow velocity). If the droplet is not moving in space (with respect to a frame of reference attached to the walls of the channel), then the relative velocity of the droplet must equal the gas-phase velocity at the droplet location, and the electric force must balance the drag force acting on the droplet. From this balance of forces, it is possible to find the strength of the electrostatic field necessary to stabilise a droplet with a given diameter and charge density. The results of such calculation for ethanol are shown in Fig. 9 as a function of the flow velocity and for different droplet diameters and charge densities. For a given droplet diameter and charge density, the strength of the electrostatic field necessary to stabilise a droplet increases with increasing flow velocity, as a consequence of the higher drag force acting on the droplet. Droplets with larger diameter (but the same charge density) generally require a lower strength of the electric field to reach stabilisation for a given flow velocity. This is a consequence of the larger net charge of the droplet (proportional to d^3, whereas the drag force for a fixed relative velocity is at maximum proportional to d^2), which requires a lower electrostatic field strength to reach a balance between the electrostatic and drag forces. Similarly, the effect of increasing the charge density is to decrease the strength of the electrostatic field necessary to reach force equilibrium. It is interesting to note that if a maximum theoretical value of the electrostatic field strength is imposed (limited e.g., by the breakdown threshold of the gas phase), the flow velocities for which the concept of electrostatic stabilisation can be implemented remain relatively low. As far as the ambient conditions are concerned, it is noted that the strength of the electrostatic field to reach force equilibrium increases with increasing pressure and temperature of the gas phase (higher drag force). Note that the ambient conditions affect the drag force through the gas-phase density and dynamic viscosity, whereas the type of fuel affects the drag force by changing the properties of the gas film around the evaporating droplet [34] (film conditions also depend on the ambient temperature). If the polydisperse nature of a spray is considered, and

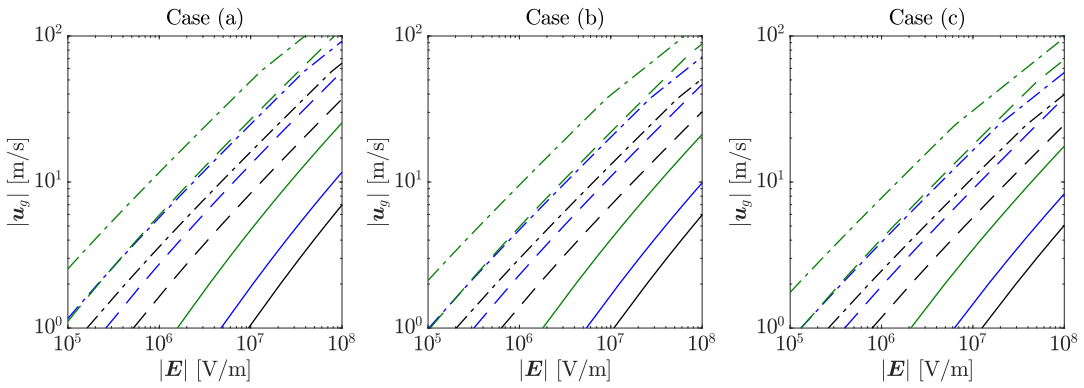

Fig. 9. External electrostatic field strengths required to achieve droplet stabilisation as a function of the gas-phase velocity at the three ambient conditions investigated in this work for ethanol droplets with the diameters: d = 10 μm ——, d = 50 μm — —, and d = 100 μm – · –. Different colours indicate different charge densities: black lines for $|\rho_{q,d}|$ = 0.5 C/m^3, blue lines for $|\rho_{q,d}|$ = 1 C/m^3, green lines for $|\rho_{q,d}|$ = 3 C/m^3. These results have been obtained by using Eqs. (1) and (2) and imposing $\boldsymbol{F}_E + \boldsymbol{F}_D = 0$ with $\boldsymbol{u}_{\text{rel}} = \boldsymbol{u}_g$. An external electrostatic field aligned with the gas-phase velocity is implicitly assumed. $T_d = T_{d,\text{eq}}$ is also assumed for all droplets. (For interpretation of the references to colour in this figure legend, the reader is referred to the web version of this article.)

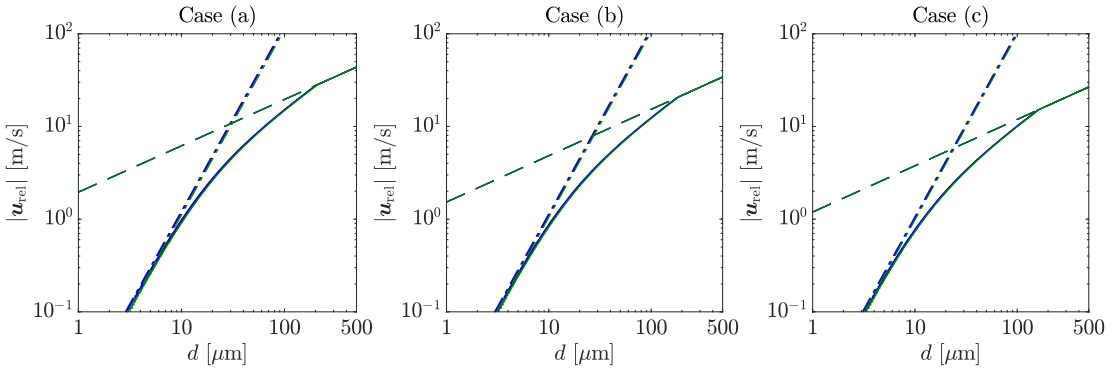

Fig. 10. Relative velocity required to achieve droplet stabilisation as a function of the droplet diameter at $|\boldsymbol{E}| = 1.5\times10^6$ V/m and $|\rho_{q,d}| = 3$ C/m^3 for the three ambient conditions investigated in this work. The drag force was calculated by using C_D according to Eq. (3) ——, C_D with a constant value of 0.424 — —, or by directly invoking Stokes' law (i.e., $C_D = 24/\text{Re}_d$) – · –. The three fuels are indicated by different colours: black for ethanol, blue for n-heptane and green for n-decane. $T_d = T_{d,\text{eq}}$ is assumed for all droplets. (For interpretation of the references to colour in this figure legend, the reader is referred to the web version of this article.)

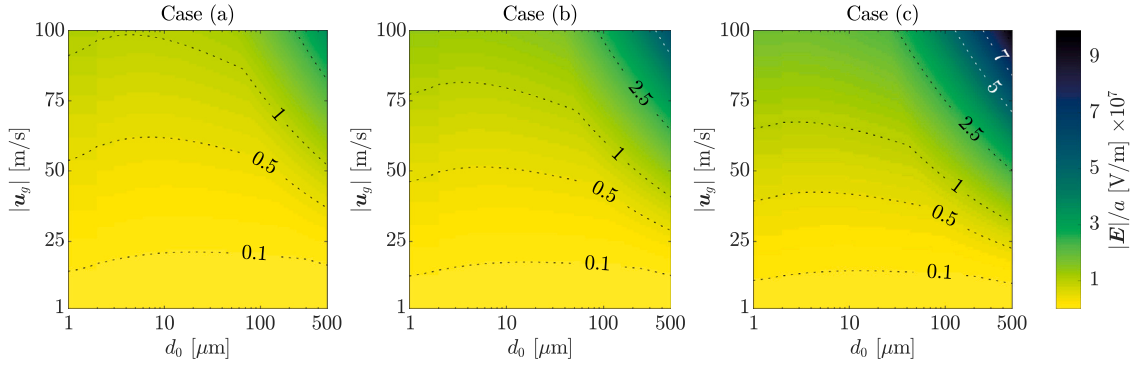

Fig. 11. Maps of the external electrostatic field strength (scaled by the constant a) required to achieve droplet stabilisation as a function of the gas-phase velocity and droplet diameter for ethanol at the three ambient conditions investigated in this work and using a net charge of the droplet equal to q_0^*/a. Droplets with initial diameter d_0 are considered and the equilibrium is evaluated at the end of the heat-up period assuming $d \approx d_0$ and $T_d = T_{d,\text{eq}}$.

assuming a uniform charge density across all droplets, only droplets with a specific diameter can be stabilised for a given flow velocity and electrostatic field strength. This is further demonstrated in Fig. 10, where the relative velocity necessary to stabilise a droplet as a function of its diameter for a selected electrostatic field strength and droplet charge density is shown. Results for all three fuels investigated in this work are reported. Assuming an electrostatic force aligned with the gas-phase velocity, every horizontal line $|\boldsymbol{u}_g| = |\boldsymbol{u}_{\text{rel}}|$ indicates the diameter for which equilibrium is reached, separating the spray into two distinct regions. Droplets with diameters falling in the top area will move upstream, whereas droplets with diameters in the region below the line will move downstream, as also observed in Ref. [16]. The results also demonstrate that the relative velocities necessary to achieve spatial equilibrium of the droplets are similar for all fuels investigated in this work. The implications of the fuel type on the trajectory of the droplets will be further discussed in Section 4.4.

The strength of the electrostatic field necessary to balance the drag force in the case of $q_d = q_0^*/a$ is shown in Fig. 11, as a function of the droplet diameter and gas-phase velocity. The equilibrium between the drag and electrostatic forces is evaluated at the conditions immediately

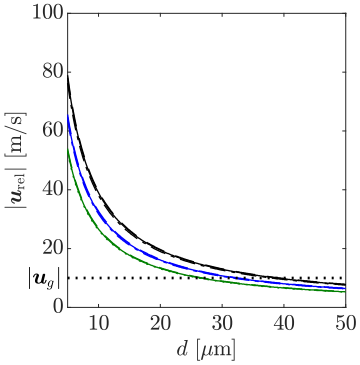

Fig. 12. Relative velocity required to achieve droplet stabilisation for a single, evaporating droplet with initial diameter $d_0 = 50$ µm and initial charge density $|\rho_{q,d,0}| = 3$ C/m^3 at $|\boldsymbol{E}| = 1.5 \times 10^6$ V/m. Each fuel is distinguished as: ethanol ——, n-heptane — —, and n-decane — · —. Colours indicate the three ambient conditions investigated in this work: black lines for Case (a), blue lines for Case (b), green lines for Case (c). Results were obtained by imposing a constant droplet net charge equal to the initial value $q_d = \pi d_0^3 \rho_{q,d,0}/6$. (For interpretation of the references to colour in this figure legend, the reader is referred to the web version of this article.)

after the droplet heat-up period, such that the droplet diameter is still equal to d_0 and the droplet temperature is equal to $T_{d,\rm eq}$ (consistent with the evaporation model used in this study). Note that the strength of the electrostatic field reported in Fig. 11 is scaled by a. Only ethanol fuel, at the three ambient conditions investigated in this work, is considered. It is interesting to note that for low values of the flow velocity, the strength of the electrostatic field to reach a balance between the drag and electrostatic forces becomes almost independent of the droplet size. This is due to the fact that for intermediate droplet diameters, the increase of the drag force (proportional to d_0 for very low Re_d and to d_0^2 for high Re_d) with increasing droplet diameter is counterbalanced by an almost equal increase of the net charge (proportional to $d_0^{3/2}$). Therefore, a given electrostatic field strength could enable stabilisation (or quasi-stabilisation) of a range of droplet diameters. This range becomes narrower with increasing gas-phase velocity. In addition, we note that the electrostatic field strength required to balance the drag force increases from Case (a) to Case (c) as a consequence of the increase in drag force with increasing gas density and dynamic viscosity. Equivalent maps for the other fuels considered in this work (not shown here) look very similar to the ones shown in Fig. 11 for ethanol. Small deviations are due to the differences in surface tension between the fuels at the droplet injection temperature (cf. Fig. 2), which lead to different values of q_d, and to differences in the viscosity of the gas film around the droplet, which affect the drag coefficient. Note that the fuel with the highest surface tension is also capable of holding the highest net charge, which implies a lower electrostatic field strength required to reach force equilibrium. It is clear at this point that the main uncertainty is related to the evaluation of the actual value of the net charge within a given droplet. Future research should focus on understanding whether this net charge is dependent on the fuel type and droplet size. If the net charge after atomisation is $q_d = q_0^*/a$, with a independent of the fuel type and droplet size, then the proposed droplet stabilisation mechanism could be used for multiple fuels, i.e., fuel flexibility could be achieved.

4.4. Droplet trajectories

We conclude our analysis by investigating the fuel effects on the droplet trajectories in a channel flow. A specified case with a gas-phase velocity of $|\boldsymbol{u}_g| = 10$ m/s, $d_0 = 50$ µm, $|\boldsymbol{E}| = 1.5 \times 10^6$ V/m, and $|\rho_{q,d,0}| = 3$ C/m^3 is considered as reference. Since the initial charge density and diameter of the droplets are given, the net charge of the droplets is the same for all the fuels. The type of fuel affects the initial

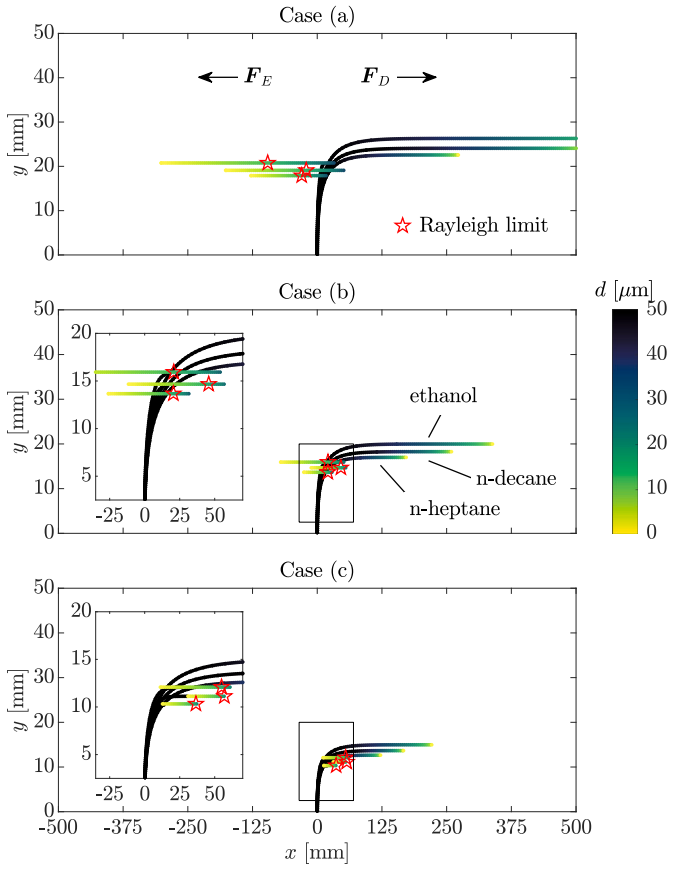

Fig. 13. Single droplet ($d_0 = 50$ µm) trajectories with evaporation in a bulk flow velocity of 10 m/s when applying either no electrostatic forces (i.e., $\boldsymbol{F}_E = 0$ N) or using $|\boldsymbol{E}| = 1.5 \times 10^6$ V/m and $|\rho_{q,d,0}| = 3$ C/m^3 for the various fuels at the three ambient conditions investigated in this work. The red star symbols indicate the location in each trajectory where the Rayleigh limit is reached (for the cases with an electrostatic force). (For interpretation of the references to colour in this figure legend, the reader is referred to the web version of this article.)

mass of the droplet, the evaporation rate, the drag force through the properties of the film around the droplet, and the critical diameter (onset of the Rayleigh instability). It should be noted that, as also marked in Fig. 12, the equilibrium relative velocity for the initial diameter used in the present case is slightly lower than the imposed gas-phase velocity for all the investigated fuels. Therefore, we expect the droplet to initially move downstream immediately after injection. As the droplet evaporates, the charge density increases (constant net charge assumption). For sufficiently small droplets, the relative velocity required to maintain an equilibrium between the drag and electrostatic forces becomes higher than the imposed gas-phase velocity (cf. Fig. 12), which implies upstream movement of the droplet. Note also that the equilibrium relative velocity is similar for all the fuels and decreases with increasing ambient pressure, i.e. moving from Case (a) to Case (c). Therefore, the upstream movement of the droplets is expected to be more evident in the low-pressure cases. The resulting droplet trajectories for all the fuels in the three ambient conditions investigated in this work are shown in Fig. 13, with and without the influence of electrostatic forces. Red star symbols mark the location where the Rayleigh limit is reached and charge-induced secondary breakup is expected. In all cases, it is demonstrated that the applied electrostatic forces are sufficient to confine droplet evaporation within a relatively narrow region close to the injection location before the onset of charge-induced secondary breakup. As the droplet diameter decreases, a strong acceleration in the negative x-direction is observed as a consequence of the reduction of the drag force (the net charge of the droplet is assumed

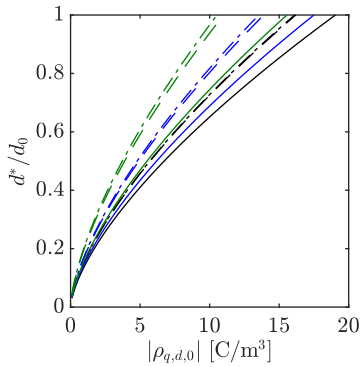

Fig. 14. Non-dimensional critical diameter, d^*/d_0, for a droplet with initial diameter $d_0 = 50$ μm as a function of the initial droplet charge density, $|\rho_{q,d,0}|$. Each fuel is distinguished as: ethanol ——, n-heptane — —, n-decane – · –. Colours indicate the different ambient conditions: black lines for Case (a), blue lines for Case (b), green lines for Case (c). The critical diameter has been computed by evaluating the fuel surface tension at the droplet equilibrium temperature. (For interpretation of the references to colour in this figure legend, the reader is referred to the web version of this article.)

to not change during evaporation; therefore, the electrostatic force is constant). The space necessary to complete evaporation decreases with increasing temperature of the gas phase (i.e., moving from Case (a) to Case (c)) due to the higher evaporation rate constant. It is also interesting to note that the penetration of the droplets in the y-direction depends on the fuel type. The final location along the y-axis is mainly the result of the temporal evolution of the droplet mass; therefore, it depends on the initial mass (density of the fuel at the injection temperature) and the evaporation dynamics (heat-up period and evaporation rate constant). Overall, ethanol droplets tend to penetrate more in the vertical direction, whereas n-heptane droplets show the least penetration. Note that for different values of the initial droplet charge density, similar trajectories can be obtained through an adequate choice of the strength of the external electrostatic field, with the only difference being the diameter at which the Rayleigh limit is reached (see Fig. 5).

Similar considerations also apply in the case of a droplet net charge equal to a fraction of the critical charge at injection, i.e., $q_d = q_0^*/a$. Given that the net charge is very similar for all the fuels (see Fig. 6 and related comments), trajectories similar to the results shown in Fig. 13 can be obtained with a proper adjustment of the electrostatic field strength (e.g., based on the maps shown in Fig. 11). Also in this case, for each ambient condition and for a given initial droplet diameter, the critical diameter, d^*, at which the Rayleigh limit is reached depends only on the initial droplet charge density, i.e., on the choice of a (see also Eq. (6) and Table 2) and the fuel type. For reference, Fig. 14 shows the critical diameter for the various fuels and ambient conditions investigated in this work as a function of the initial droplet charge density. Note that the data in Fig. 14 refers to the specific initial droplet diameter used for the trajectories reported in Fig. 13. The critical diameter increases with increasing initial droplet charge density (i.e., lower values of a). In addition, d^* increases from Case (a) to Case (c) for all the fuels. It is important to note that the hydrocarbon fuels, which tend to have higher critical diameters compared to ethanol, show very similar values of d^*, which could become relevant in the context of fuel flexibility.

The axial movement of the droplets can be controlled by modulating the strength of the electrostatic field. This is demonstrated in Fig. 15, where the minimum and maximum x location of the droplet trajectories, from injection until the Rayleigh limit is reached, is shown as a function of the strength of the electrostatic field. Results for d_0 equal to 50 μm and 100 μm (with a bulk flow velocity of 10 m/s and $|\rho_{q,d,0}| = 3$ C/m^3) are shown, together with a case with lower velocity of the carrier phase and a case with a higher initial droplet charge density. It is clear from Fig. 15 that for each ambient condition, the axial movement of the droplet tends to be more confined close to the injection location for intermediate values of the strength of the electrostatic field. In addition, the axial movement is much more sensitive to the strength of the electrostatic field at low-pressure ambient conditions (Case (a)) compared to high-pressure ambient conditions (e.g., Case (c)). The axial movement is in general larger for ethanol, which is characterised by a larger evaporation time and lower values of the critical diameter (cf. Fig. 14). The strength of the electrostatic field to achieve droplet stabilisation decreases with increasing initial droplet diameter (for the same value of the initial droplet charge density) as already observed with reference to Fig. 9. An increase in initial droplet diameter also results in a higher sensitivity of the axial movement of the droplet to changes in the strength of the electrostatic field. Similar considerations can also be made for lower bulk flow velocities and higher initial droplet charge densities. Both a decrease in the flow bulk velocity and an increase in the initial droplet charge density result in a lower strength of the electrostatic field necessary to achieve a confined evaporation, as well as a higher sensitivity of the droplet axial location to the strength of the electrostatic field (see also Fig. 9).

Secondary breakup induced by charge repulsion is not the only mechanism that could lead to droplet fragmentation. It is also important to evaluate the breakup induced by aerodynamic interactions [58]. Different aerodynamic breakup regimes can be distinguished on the basis of the Weber number of the droplet, $\mathrm{We} = \rho_g|\boldsymbol{u}_{\mathrm{rel}}|^2 d/\sigma$. For droplets characterised by a low Ohnesorge number, significant fragmentation is observed starting from $\mathrm{We} = 12$, which is the threshold for the so-called bag breakup [58]. Larger values of We make the fragmentation even more intense (up to the catastrophic breakup regime), whereas for $\mathrm{We} < 12$, only vibrational breakup is expected. The latter is the least effective breakup regime and generally does not lead to the formation of small droplets, but rather fragments of size comparable with the parent droplet. When electrosprays are used, it is important to evaluate which mechanism of breakup, charge-induced or aerodynamic-induced, occurs first. It should also be noted that the presence of charges reduces the stabilising effect of surface tension, which may anticipate the aerodynamic-induced breakup. As suggested in Ref. [18], this could be taken into account by defining a corrected Weber number $\mathrm{We}^* = \rho_g|\boldsymbol{u}_{\mathrm{rel}}|^2 d/(\sigma - q_d^2/(8\pi^2\epsilon_0 d^3))$. Fig. 16 shows the time evolution (from injection) of We and We* corresponding to the trajectories reported in Fig. 13. The occurrence of the Rayleigh limit is also marked, which corresponds to a vertical asymptotic behaviour for We*. It can be determined that in this specific case, the dominant breakup effect is driven by charge repulsion and possibly triggered by aerodynamic interactions as demonstrated by the rapid increase of We* in the vicinity of the Rayleigh limit. However, it is important to note that in Case (c) (high gas pressure and temperature), the We number immediately after injection is slightly above the bag breakup threshold, which could lead to early droplet fragmentation. It should be noted that these results depend on the injection conditions (initial droplet diameter and injection velocity), on the type of fuel, and on the gas-phase conditions (velocity, pressure, and temperature). Therefore, careful evaluations should be made in each specific configuration.

5. Summary and conclusions

The effects of fuel type on the electrohydrodynamic control of charged droplets were numerically investigated. The considered configuration combines the use of an electrospray and an external electrostatic field to counteract the drag force induced by the flow, and provides a basis for the development of new technologies towards enhanced fuel preparation and fuel flexibility in liquid-fuelled combustion systems. The characteristics of three different fuels, namely ethanol, n-heptane, and n-decane, were studied in various ambient conditions relevant to gas turbine applications. It was shown that the critical droplet diameter for charge-induced breakup, given by the Rayleigh

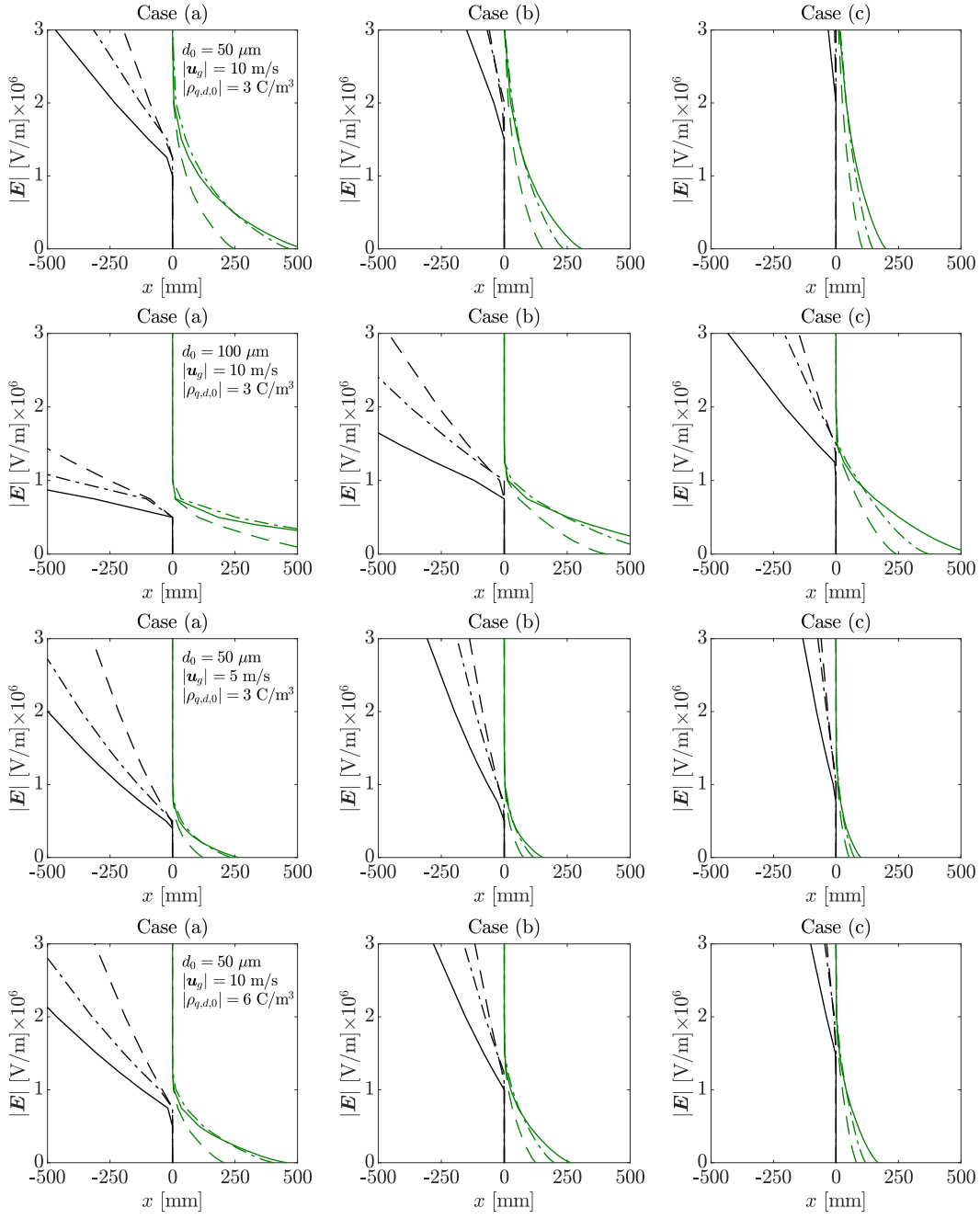

Fig. 15. Minimum (black lines) and maximum (green lines) x location of an evaporating droplet as a function of the strength of the electrostatic field. The fuels are indicated by different lines: ethanol ——, n-heptane — —, n-decane – · –. Each row is reporting results for different conditions: First row for d_0 = 50 μm, bulk velocity of 10 m/s, and $|\rho_{q,d,0}|$ = 3 C/m^3; Second row for d_0 = 100 μm, bulk velocity of 10 m/s, and $|\rho_{q,d,0}|$ = 3 C/m^3; Third row for d_0 = 50 μm, bulk velocity of 5 m/s, and $|\rho_{q,d,0}|$ = 3 C/m^3; Fourth row for d_0 = 50 μm, bulk velocity of 10 m/s, and $|\rho_{q,d,0}|$ = 6 C/m^3. The droplet trajectories considered for this plot are from injection until the time when the Rayleigh limit is reached. (For interpretation of the references to colour in this figure legend, the reader is referred to the web version of this article.)

limit for droplet stability, is strongly dependent on the fuel type for the three fuels and the three ambient conditions investigated in this work. Furthermore, the results suggest that the droplet temperature at injection could be used as a parameter to control the onset of this secondary breakup, if the droplet net charge is fixed to a given fraction of the maximum possible charge. This could also enable the control of the fraction of the initial droplet mass that undergoes charged-induced breakup.

The implications of the above findings on the modulation of the droplet trajectories were investigated through the study of a canonical electrospray in crossflow configuration. The objective was to stabilise the injected droplets within a confined region by counteracting the drag force induced by the bulk flow. This enables full pre-evaporation of the fuel before the droplets reach the flame zone. Operational maps were presented for a range of bulk flow velocities, droplet diameters, and droplet charge densities to facilitate the selection of the external electrostatic field strength required to balance the drag and electrostatic forces. Limited by the electrical breakdown threshold of the carrier phase, such balance may only be achieved for relatively low bulk flow velocities. When assuming equal charge densities and droplet sizes, the effect of fuel type on the balance of forces is negligible. In addition, if the charge at injection is assumed to be a fraction of the Rayleigh limit, the strength of the electrostatic field that balances the drag was also found to be largely independent of the initial droplet

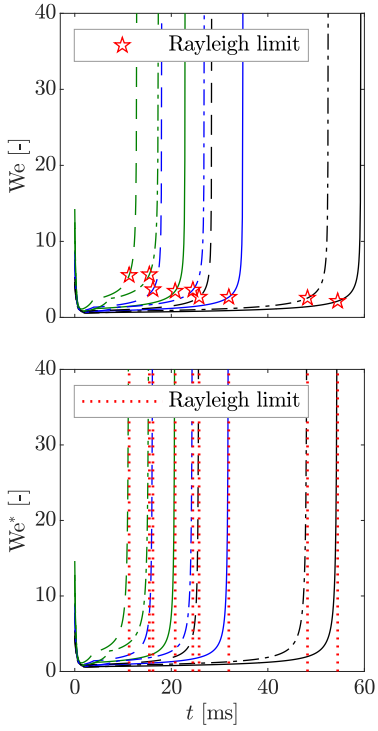

Fig. 16. Temporal evolution of the Weber number (We, top) and corrected Weber number (We*, bottom) of a single, evaporating droplet with initial diameter $d_0 = 50$ µm and initial charge density $|\rho_{q,d,0}| = 3$ C/m^3 in a bulk flow velocity of 10 m/s and using $|\boldsymbol{E}| = 1.5 \times 10^6$ V/m. Each fuel is distinguished as: ethanol ——, n-heptane — —, n-decane — · —. Colours indicate the different ambient conditions: black lines for Case (a), blue lines for Case (b), green lines for Case (c). The red star symbols (top) and red dotted lines (bottom) mark the time instant when the Rayleigh limit is reached. (For interpretation of the references to colour in this figure legend, the reader is referred to the web version of this article.)

diameter for intermediate droplet sizes. Finally, it was demonstrated that with identical electrostatic fields, and despite being affected by the individual evaporation rates of each fuel, (targeted) evaporation within a confined region can be achieved for all the fuels and ambient conditions studied in this work. The axial movement of the droplets can be controlled by modulating the strength of the electrostatic field. The sensitivity of the axial movement of the droplets to changes in the strength of the electrostatic field increases with decreasing bulk flow velocity and increasing initial droplet diameter and initial droplet charge density.

CRediT authorship contribution statement

Andrea Giusti: Writing – review & editing, Writing – original draft, Visualization, Validation, Software, Methodology, Investigation, Formal analysis, Data curation, Conceptualization. **Daniel Fredrich:** Writing – review & editing, Writing – original draft, Visualization, Validation, Software, Methodology, Investigation, Formal analysis, Data curation, Conceptualization.

Declaration of competing interest

The authors declare that they have no known competing financial interests or personal relationships that could have appeared to influence the work reported in this paper.

Data availability

Data will be made available on request.

Acknowledgements

The single droplet solver used in this work was initially developed by Dr Giulio Borghesi, who is deeply acknowledged for sharing the source code.

Appendix. Estimation of droplet Reynolds number effects on evaporation

To include the effects of a relative velocity between the gas and the droplet on the evaporation rate, the droplet diameter is computed by integrating the following equation together with the equation for the droplet velocity:

$$\frac{\mathrm{d}d}{\mathrm{d}t} = -\frac{K'}{2d}, \tag{A.1}$$

where K' is a corrected evaporation rate 'constant' that includes Re_d effects. K' has been obtained by combining the Frössling correlation for mass transfer under forced convection and the evaporation rate constant, K, obtained for a quiescent medium under the assumption of equilibrium between heat and mass transfer with the surroundings. Assuming the droplet diameter to be constant during the heat-up period, K' can be expressed as:

$$K' = \begin{cases} 0, & \text{if } t < \tau_{\mathrm{hp}}, \\ K\left(1 + 0.276\mathrm{Pr}^{1/3}\mathrm{Re}_d^{1/2}\right), & \text{otherwise}, \end{cases} \tag{A.2}$$

where Pr is the Prandtl number, taken equal to 0.7. K and τ_{hp} have been evaluated with the same methodology discussed in Section 3.2. The integration of Eq. (A.1) is performed by considering a variable Re_d, which is updated at every integration step to take into account changes in diameter, dynamic viscosity, and relative velocity. It should be noted that the presence of a relative velocity between the gas and the droplet also enhances the heat transfer, leading to a shorter heat-up period. A correction to the duration of the heat-up period is not applied for the evaluations performed in this section.

Fig. A.17 shows the trajectories of droplets obtained with the evaporation formulation described above. Simulations have been performed at the same conditions used for the results discussed in Section 4.4 (with the only difference being the inclusion of Re_d effects into the evaporation rate constant). By comparing Fig. 13 with Fig. A.17, it is clear that the main effect of a relative velocity between the droplet and the gas is to decrease the droplet lifetime. Droplets are confined in a narrower region when the effects of the relative velocity on the evaporation rate are considered, making the use of external electrostatic fields to stabilise the droplets in the vicinity of the injection location even more effective.

The observed increase of the evaporation rate is particularly strong when an electrostatic force is applied on the droplets. The stabilisation of droplets at a fixed location increases the relative velocity between the gas and the droplets, leading to a high droplet Reynolds number [16]. This is demonstrated in Fig. A.18, which shows the temporal evolution of Re_d corresponding to the trajectories of the ethanol droplets shown in Fig. A.17. Note that the evolution of Re_d for the other fuels (not shown here) shows trends similar to ethanol. In the case without an external electrostatic field, Re_d is high immediately after injection (because of the vertical injection velocity), and then quickly decreases to very small values, which characterise a droplet with a strong tendency to follow the bulk flow. When an external electrostatic field is applied, Re_d remains relatively high even a long time after injection, as a consequence of the balance between the drag and electrostatic forces, which stabilises the droplets in space. Therefore, droplet stabilisation also has the effect of increasing the evaporation rate, which could be exploited to further improve the fuel preparation process.

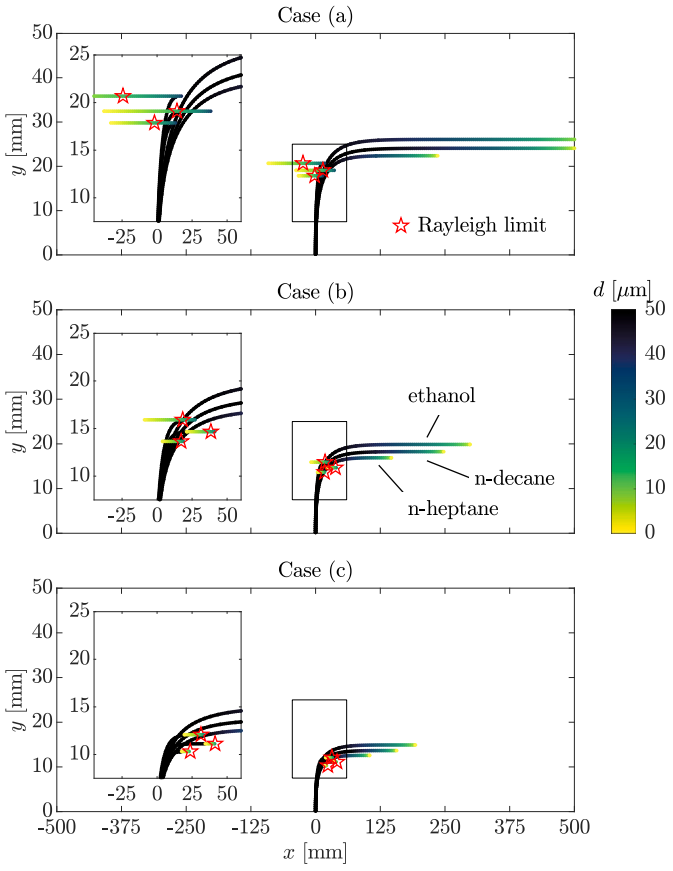

Fig. A.17. Single droplet (d_0 = 50 μm) trajectories with evaporation in a bulk flow velocity of 10 m/s when applying either no electrostatic forces (i.e., $\boldsymbol{F}_E = 0$ N) or using $|\boldsymbol{E}| = 1.5 \times 10^6$ V/m and $|\rho_{q,d,0}| = 3$ C/m^3 for the various fuels at the three ambient conditions investigated in this work. The evaporation rate constant is corrected based on the droplet Reynolds number according to Eq. (A.2). The red star symbols indicate the location in each trajectory where the Rayleigh limit is reached (for the cases with an electrostatic force). (For interpretation of the references to colour in this figure legend, the reader is referred to the web version of this article.)

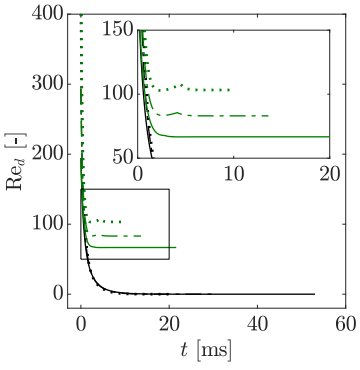

Fig. A.18. Temporal evolution of the droplet Reynolds number of a single, evaporating ethanol droplet (d_0 = 50 μm) in a bulk flow velocity of 10 m/s at the three ambient conditions investigated in this work: Case (a) ——, Case (b) – · –, Case (c) ·····. Black lines: no electrostatic forces (i.e., $\boldsymbol{F}_E = 0$ N); green lines: $|\boldsymbol{E}| = 1.5 \times 10^6$ V/m and $|\rho_{q,d,0}| = 3$ C/m^3. Note that for simulations without electrostatic forces there is a strong overlap between the three cases. (For interpretation of the references to colour in this figure legend, the reader is referred to the web version of this article.)

References

[1] ITF. The potential of E-fuels to decarbonise ships and aircraft. International Transport Forum Policy Papers, (111). OECD Publishing, Paris; 2023.

[2] Masri A. Challenges for turbulent combustion. Proc Combust Inst 2021;38(1):121–55.

[3] Vranos A. Turbulent mixing and NOx formation in gas turbine combustors. Combust Flame 1974;22(2):253–8.

[4] de Oliveira PM, Fredrich D, De Falco G, El Helou I, D'Anna A, Giusti A, et al. Soot-free low-NOx aeronautical combustor concept: The lean azimuthal flame for kerosene sprays. Energy Fuels 2021;35(9):7092–106.

[5] Reitz RD. Directions in internal combustion engine research. Combust Flame 2013;160(1):1–8.

[6] Jenny P, Roekaerts D, Beishuizen N. Modeling of turbulent dilute spray combustion. Prog Energy Combust Sci 2012;38(6):846–87.

[7] Martin JW, Salamanca M, Kraft M. Soot inception: Carbonaceous nanoparticle formation in flames. Prog Energy Combust Sci 2022;88:100956.

[8] Hill S, Douglas Smoot L. Modeling of nitrogen oxides formation and destruction in combustion systems. Prog Energy Combust Sci 2000;26(4):417–58.

[9] Sun J, Caton JA, Jacobs TJ. Oxides of nitrogen emissions from biodiesel-fuelled diesel engines. Prog Energy Combust Sci 2010;36(6):677–95.

[10] Mastorakos E. Ignition of turbulent non-premixed flames. Prog Energy Combust Sci 2009;35(1):57–97.

[11] Lacoste DA. Flames with plasmas. Proc Combust Inst 2023;39(4):5405–28.

[12] Starikovskiy A, Aleksandrov N. Plasma-assisted ignition and combustion. Prog Energy Combust Sci 2013;39(1):61–110.

[13] Ju Y, Sun W. Plasma assisted combustion: Dynamics and chemistry. Prog Energy Combust Sci 2015;48:21–83.

[14] Ren Y, Cui W, Li S. Electrohydrodynamic instability of premixed flames under manipulations of dc electric fields. Phys Rev E 2018;97:013103.

[15] Xiong Y, Cha MS, Chung SH. AC electric field induced vortex in laminar coflow diffusion flames. Proc Combust Inst 2015;35(3):3513–20.

[16] Fredrich D, Weiand E, Giusti A. Electrostatic fields for the control of evaporating charged fuel sprays. Int J Multiph Flow 2023;160:104312.

[17] Thomas M, Elliott A, Guimond DP. Electrostatic fuel atomisation for gas turbines. Technical Report WP-1184, Naval Surface Warfare Centre; 2006.

[18] Shrimpton JS, Laoonual Y. Dynamics of electrically charged transient evaporating sprays. Internat J Numer Methods Engrg 2006;67(8):1063–81.

[19] Lord Rayleigh FRS. XX. On the equilibrium of liquid conducting masses charged with electricity. London Edinb Dublin Philos Magaz J Sci 1882;14(87):184–6.

[20] Shrimpton J, Yule A. Characterisation of charged hydrocarbon sprays for application in combustion systems. Exp Fluids 1999;26(5):460–9.

[21] Al-Ahmad G, Shrimpton JS, Ergene EL, Mashayek F. Electrical performance of a charge-injection atomizer using viscous organic oils. Atomization Sprays 2009;19(6):547–66.

[22] Ahmed T, Kourmatzis A, Masri AR. Atomization behaviour of a hybrid air-blast-electrostatic atomizer for spray combustion. Fuel 2021;288:119716.

[23] Anderson EK, Koch JA, Kyritsis DC. Phenomenology of electrostatically charged droplet combustion in normal gravity. Combust Flame 2008;154(3):624–9.

[24] Ahmed T, Kourmatzis A, Singh G, Masri AR. Turbulent spray flames of kerosene issuing from a hybrid electrohydrodynamic-air-blast atomiser. Combust Flame 2022;239:111573, A dedication to Professor Kenneth Noel Corbett Bray.

[25] Kelly AJ. The electrostatic atomization of hydrocarbons. 1984.

[26] Yule A, Shrimpton J, Watkins A, Balachandran W, Hu D. Electrostatically atomized hydrocarbon sprays. Fuel 1995;74(7):1094–103.

[27] Rigit ARH, Shrimpton JS. Estimation of the diameter–charge distribution in polydisperse electrically charged sprays of electrically insulating liquids. Exp Fluids 2006;46:1159–71.

[28] Shrimpton JS, Yule AJ. Drop size and velocity measurements in an electrostatically produced hydrocarbon spray. J Fluids Eng 1998;120(3):580–5.

[29] Malkawi G, Yarin AL, Mashayek F. Breakup mechanisms of electrostatic atomization of corn oil and diesel fuel. J Appl Phys 2010;108(6):064910.

[30] Correa SM. Power generation and aeropropulsion gas turbines: From combustion science to combustion technology. Symposium (Int) Combust 1998;27(2):1793–807.

[31] Kyritsis DC. Electrostatically manipulated flames for compact heat generation. 2020, US Patent 10,677,455 B2.

[32] Doyle A, Moffett DR, Vonnegut B. Behavior of evaporating electrically charged droplets. J Colloid Sci 1964;19(2):136–43.

[33] Faeth G. Evaporation and combustion of sprays. Prog Energy Combust Sci 1983;9(1):1–76.

[34] Yuen MC, Chen LW. On drag of evaporating liquid droplets. Combust Sci Technol 1976;14(4–6):147–54.

[35] Kadoya K, Matsunaga N, Nagashima A. Viscosity and thermal conductivity of dry air in the gaseous phase. J Phys Chem Ref Data 1985;14(4):947–70.

[36] Reichenberg D. New methods for the estimation of the viscosity coefficients of pure gases at moderate pressures (with particular reference to organic vapors). AIChE J 1975;21(1):181–3.

[37] Green DW, Perry RH. Perry's chemical engineer's handbook. 8th ed.. Mc Graw Hill; 2008.

[38] Wilke CR. A viscosity equation for gas mixtures. J Chem Phys 2004;18(4):517–9.

[39] Poling BE, Prausnitz JM, O'Connell JP. Properties of gases and liquids. fifth ed.. New York: McGraw-Hill Education; 2001.

[40] Abramzon B, Sirignano W. Droplet vaporization model for spray combustion calculations. Int J Heat Mass Transfer 1989;32(9):1605–18.
[41] Abramzon B, Sazhin S. Droplet vaporization model in the presence of thermal radiation. Int J Heat Mass Transfer 2005;48(9):1868–73.
[42] Renksizbulut M, Yuen MC. Numerical study of droplet evaporation in a high-temperature stream. J Heat Transfer 1983;105(2):389–97.
[43] Fredrich D, Giusti A. Numerical investigation of multi-component droplet evaporation and autoignition for aero-engine applications. Combust Flame 2022;241:112023.
[44] Kourmatzis A. Sensitivities in the modeling of electrostatically charged droplet evaporation and combustion. J Energy Eng 2017;143(3):04016060.
[45] Borghesi G, Mastorakos E. Spontaneous ignition of isolated n-heptane droplets at low, intermediate, and high ambient temperatures from a mixture-fraction perspective. Combust Flame 2015;162(6):2544–60.
[46] Borghesi G, Mastorakos E. Utoignition of n-decane droplets in the low-, intermediate-, and high-temperature regimes from a mixture fraction viewpoint. Flow Turbul Combust 2016;96:1107–21.
[47] Pinheiro AP, Vedovoto JM, da Silveira Neto A, van Wachem BG. Ethanol droplet evaporation: Effects of ambient temperature, pressure and fuel vapor concentration. Int J Heat Mass Transfer 2019;143:118472.
[48] Kitano T, Nishio J, Kurose R, Komori S. Effects of ambient pressure, gas temperature and combustion reaction on droplet evaporation. Combust Flame 2014;161(2):551–64.
[49] Gonçalves F, Trindade A, Costa C, Bernardo J, Johnson I, Fonseca I, et al. PVT, viscosity, and surface tension of ethanol: New measurements and literature data evaluation. J Chem Thermodyn 2010;42(8):1039–49.
[50] Brock JR, Bird RB. Surface tension and the principle of corresponding states. AIChE J 1955;1(2):174–7.
[51] Mohsen-Nia M, Rasa H, Naghibi S. Experimental and theoretical study of surface tension of n-pentane, n-heptane, and some of their mixtures at different temperatures. J Chem Thermodyn 2010;42(1):110–3.
[52] Kebarle P, Peschke M. On the mechanisms by which the charged droplets produced by electrospray lead to gas phase ions. Anal Chim Acta 2000;406(1):11–35.
[53] Agathou MS, Kyritsis DC. Electrostatic atomization of hydrocarbon fuels and bio-alcohols for engine applications. Energy Convers Manage 2012;60:10–7, Special issue of Energy Conversion and Management dedicated to ECOS 2011 - the 24th International Conference on Efficiency, Costs, Optimization, Simulation and Environmental Impact of Energy Systems.
[54] Massachusetts Institute of Technology. Lecture notes of space propulsion; session 22-23: Cone-jet electrosprays, or colloid thrusters. 2015, URL https://ocw.mit.edu/courses/16-522-space-propulsion-spring-2015/resources/mit16_522s15_lecture22-23/.
[55] Shrimpton J. Dielectric charged drop break-up at sub-Rayleigh limit conditions. IEEE Trans Dielectr Electr Insulat 2005;12(3):573–8.
[56] Singh G, Pham P, Kourmatzis A, Masri A. Effect of electric charge and temperature on the near-field atomization of diesel and biodiesel. Fuel 2019;241:941–53.
[57] Rigit ARH, Shrimpton JS. Electrical performance of charge injection electrostatic atomizers. Atomization Sprays 2006;16(4):401–20.
[58] Guildenbecher DR, López-Rivera C, Sojka PE. Secondary atomization. Exp Fluids 2009;46:371–402.